

Please note! This is a self-archived version of the original article.

Huom! Tämä on rinnakkaistalenne.

To cite this Article / Käytä viittauksessa alkuperäistä lähdettä:

Valtonen, L., Saari, S. & Pursiainen, S. (2021) A matrix-free fixed-point iteration for inverting cascade impactor measurements with instrument's sensitivity kernels and hardware. *Inverse Problems in Science and Engineering*, 29:13, 3261-3278.

DOI: <https://doi.org/10.1080/17415977.2021.1985489>

ARTICLE TEMPLATE

## A Matrix-Free Fixed-Point Iteration for Inverting Cascade Impactor Measurements with Instrument's Sensitivity Kernels and Hardware

Laura Valtonen<sup>a</sup> Sampo Saari<sup>b</sup>, and Sampsa Pursiainen<sup>a</sup>

<sup>a</sup>Mathematics and statistics, Faculty of Information Technology and Communication Science, Tampere University, PO Box 1001, 30014 Tampere, Finland; <sup>b</sup>[Pedagogical Innovations, Tampere University of Applied Sciences, Kuntokatu 3, FI-33520 Tampere, Finland.](#)

### ARTICLE HISTORY

Compiled May 19, 2021

### ABSTRACT

This study focuses on advancing the inversion of aerosol data measured by a cascade impactor. Our aim is to find and validate a comprehensive and robust mathematical model for reconstructing a particle mass distribution. In this paper, we propose a fixed-point iteration as a method for inverting cascade impactor measurements with a relatively simple measurement hardware, which is not optimized for handling advanced linear algebraic operations such as large matrices. We validate this iteration numerically against an iterative L1 norm regularized iterative alternating sequential inversion algorithm. In the numerical experiments, we investigate and compare a point-wise (matrix-free) and integrated kernel-based approach in inverting five different aerosol mass concentration distributions based on simulated measurements and sensitivity kernel functions.

### KEYWORDS

Aerosols, Cascade Impactor, Electrical Low Pressure Impactor (ELPI), Field-Programmable Gate Array (FPGA), Inverse Problems, Fixed-Point Iteration, L1-Regularization.

## 1. Introduction

This article focuses on the mathematical modelling and inversion of cascade impactor aerosol measurements. An aerosol is a finely divided mixture consisting of gaseous media and mixed liquid or solid particles. Aerosol particles are formed when liquids or solids are fined or when the gas forms particles, e.g. in burning processes. Aerosols include, for example, smoke, clouds and street dust. Today, aerosol research is an important part and growing of research on air pollution, public health, nanotechnology, medicine, atmospheric, radiological health and respiratory toxicology [1, 2].

Our example of the cascade impactors is the Electrical Low Pressure Impactor (ELPI) measuring device [3–7] which can be applied in the direct measurement of aerosol particle mass distributions, e.g., in the analysis of particulate emissions [8,9]. In ELPI, the number of particles collected by each stage can be detected by an electrometer measuring electrical currents arising from the deposition of electrically charged particles and constituting the measurement data. Another measuring principle is gravimetric, in which the impactor plates are removed and the weight of collected particle

mass are measured to get particle mass concentration distribution [1]. Reconstructing the eventual particle mass distribution based on the data is an ill-posed and ill-conditioned inverse problem [10] in which a small amount of noise in the measurements can result in a significant errors in the reconstructed mass distribution. Consequently, inverting a given set of measurements necessitates *a priori* information about the problem and regularization techniques to solve it.

Various measurement hardware solutions have typically an embedded system which utilizes the field-programmable gate array (FPGA) technology for its basic functions. The embedded FPGA platform has some computing capability which is needed for processing the data flow and can be used also to solve the present inverse problem. It is, however, not optimized for handling advanced linear algebraic operations such as large matrices [11–13] and, therefore, the inversion algorithm must be specifically designed for the hardware. The present fixed-point inversion method allows for a simple point-wise matrix-free implementation and is, therefore, attractive from the hardware point of view. Moreover, using the kernel functions as a basis for the inversion, one can find an inverse estimate via a computationally inexpensive integrated matrix formulation in which the matrix size is determined by the number of kernel functions. In the numerical experiments, we investigate and compare the point-wise and integrated approach, corresponding to characteristic set-identifier and smooth basis functions, respectively, in inverting seven different particle mass distributions based on simulated measurements and kernels.

The aim of this study is to find and validate a comprehensive and robust mathematical model for reconstructing the aerosol particle concentration distribution based on cascade impactor measurements. In particular, we will investigate a fixed-point iteration [14] which can be applied to invert the measurement data effectively with the cascade impactor measuring device. Earlier works motivating the current iterative inversion approach include, e.g., [15–18]. Here our approach is more mathematical; we justify the convergence of the proposed method based on the theory of fixed-point iterations, and evaluate the performance this iteration numerically against an iterative L1-regularized inversion algorithm. The fixed-point method regularizes the inverse problem by approaching the final estimate gradually to suppress any unwanted fluctuations in the final reconstruction. In L1-regularization, the L1 norm is utilized as a penalty function based on the *a priori* assumption that the actual distribution is well-localized, i.e., with comparably few non-zero entries. L1-regularization can be considered advantageous in reconstructing peaked distributions as it is known to yield a more focused outcome than the classical and widely-applied Tikhonov regularization technique (L2-regularized inversion) [10].

This paper is structured as follows. Section 2 introduces a mathematical forward (data prediction) model for the cascade impactor, the iterative fixed-point and L1 norm regularized inversion routines as well as the numerical experiments. The results and discussion are presented in the following Sections 3 and 4, respectively, and finally, Section 5 summarizes the findings and concludes the study. The convergence of the investigated methods has been reasoned in the Appendix.

## 2. Materials and methods

### 2.1. Inverse problem

In this paper, we investigate reconstructing a one-dimensional particle mass distribution that is a function  $g(s)$  of the logarithmic particle mass  $s \in [s_1, s_2] \subset \mathbb{R}$ . The data given consist of a set of particle masses  $\mathbf{y} = (y_1, y_2, \dots, y_m)$  measured by the cascade impactor. The masses and the aerosol distribution are related through the formula

$$y_i = \int_{s_1}^{s_2} g(s) f_i(s) ds \quad (1)$$

with  $f_1, f_2, \dots, f_m$  denoting smooth non-negative kernel functions defined on the real line  $\mathbb{R}$ . These functions represent the cascade impactor's stages, describing its sensitivity to detect particles of a given mass. The kernels are assumed to be linearly independent, i.e., the noiseless data corresponding to an identically zero aerosol distribution is assumed to vanish. Additionally, the *partition of unity* condition  $\sum_{i=1}^m f_i(s) = 1$  is satisfied for all  $s \in [s_1, s_2]$ , following from the requirement that the total particle mass captured by the cascade impactor is detected by a serially coupled set of stages. That is, the particle mass detected by the  $i$ -th sensor of the cascade impactor can be obtained by integrating the particle mass distribution  $g(s)$  multiplied by the kernel function  $f_i(s)$  over the interval  $[s_1, s_2]$ . We choose micrometer ( $\mu\text{m}$ ) as the unit of  $\exp(s)$ . The unit of  $g(s)$  is set to be micro gram per cubic meter ( $\mu\text{g}/\text{m}^3$ ).

The concentration distribution, that is, the unknown parameter of the inverse problem, is reconstructed as a superposition of linearly independent basis functions  $\varphi_1, \varphi_2, \dots, \varphi_n$  defined in  $\mathbb{R}$ , i.e.,

$$g(s) = \sum_{j=1}^n x_j \varphi_j(s), \quad \text{for all } s \in [s_1, s_2], \quad (2)$$

where  $\int_{s_1}^{s_2} \varphi_j(s) ds = 1$  for  $j = 1, 2, \dots, n$  and  $\mathbf{x} = (x_1, x_2, \dots, x_n)$  is an unknown  $n$ -component vector with  $x_i \geq 0$  for each  $j = 1, 2, \dots, n$ . The number of the basis functions  $n$  is assumed to be greater than equal to that of the kernel functions  $m$ . Substituting the discretized  $g(s)$  into equation (1) results in the formula

$$y_i = \int_{s_1}^{s_2} f_i(s) \sum_{j=1}^n x_j \varphi_j ds = \sum_{j=1}^n x_j \int_{s_1}^{s_2} f_i(s) \varphi_j ds, \quad (3)$$

which can be written in the following matrix form  $\mathbf{y} = \mathbf{A}\mathbf{x}$ , where  $\mathbf{A} = (\mathbf{f}_1, \mathbf{f}_2, \dots, \mathbf{f}_m)^T$  with  $(f_i)_j = \int_{s_1}^{s_2} f_i(s) \varphi_j(s) ds$ . The measurements are assumed to contain additive measurement noise  $\mathbf{n}$ , independent of the concentration  $\mathbf{x}$ , which leads to the following linear model:

$$\mathbf{y} = \mathbf{A}\mathbf{x} + \mathbf{n}. \quad (4)$$

Determining an estimate for the unknown coefficient vector  $\mathbf{x}$  with non-negative entries given the data  $\mathbf{y}$  is an ill-conditioned inverse problem, since  $\mathbf{x}$  is sensitive to small deviations of  $\mathbf{n}$ . Therefore, the applied inversion procedure needs to involve regularization, e.g., an iterative solver, which prevents amplification of the noise effects. In this

study, we explore two iterative regularization approaches: a fixed-point and L1 norm regularized algorithm. The vector  $\mathbf{n}$  is assumed to contain zero-mean Gaussian white (uncorrelated) noise corresponding to errors in both measurements and modelling, e.g., in the kernel functions; see, e.g., [19].

## 2.2. Fixed-point iteration

To reconstruct the distribution  $g(s)$ , we use the following fixed-point method [14]:

$$g_{k+1}(s) = \sum_{i=1}^n \frac{y_i f_i(s) g_k(s)}{\int_{s_1}^{s_2} f_i(\zeta) g_k(\zeta) d\zeta}. \quad (5)$$

As a simple iterative algorithm which converges to a fixed-point

$$g_*(s) = \sum_{i=1}^n \frac{y_i f_i(s) g_*(s)}{\int_{s_1}^{s_2} f_i(\zeta) g_*(\zeta) d\zeta} \quad (6)$$

with a relatively low number of steps, this is a fast and computationally inexpensive approach to the inversion and is particularly suitable for an environment with limited computation resources such as the measurement device itself. Substituting the approximation (2) into the formula (5) can be written in the discretized form

$$\mathbf{B} \mathbf{x}_{k+1} = \sum_{i=1}^n \frac{y^{(i)}}{\mathbf{f}_i^T \mathbf{x}_k} \mathbf{C}^{(i)} \mathbf{x}_k \quad (7)$$

and further as

$$\mathbf{x}_{k+1} = G(\mathbf{x}_k) = \mathbf{G}_k \mathbf{x}_k = \sum_{i=1}^n \frac{y^{(i)}}{\mathbf{f}_i^T \mathbf{x}_k} \mathbf{F}_i \mathbf{x}_k, \quad (8)$$

where the matrices are of the form  $\mathbf{F}_i = \mathbf{B}^{-1} \mathbf{C}_i$ , for  $i = 1, 2, \dots, n$  and can be pre-computed. The entries of  $\mathbf{B}^{-1}$  and  $\mathbf{C}_i$  are given by  $B_{\ell,j} = \int_{s_1}^{s_2} \varphi_\ell(s) \varphi_j(s) ds$ ,  $(\mathbf{C}_i)_{\ell,j} = \int_{s_1}^{s_2} f_i(s) \varphi_\ell(s) \varphi_j(s) ds$ , and  $\mathbf{G}_k = \sum_{i=1}^n \frac{y^{(i)}}{\mathbf{f}_i^T \mathbf{x}_k} \mathbf{F}_i$ . The fixed-point  $\mathbf{x}_*$  is an eigenvector of the matrix sum

$$\mathbf{G}_* = \sum_{i=1}^n \frac{y^{(i)}}{\mathbf{f}_i^T \mathbf{x}_*} \mathbf{F}_i \quad (9)$$

corresponding to the eigenvalue one, that is, it satisfies the condition

$$(\mathbf{I} - \mathbf{G}_*) \mathbf{x}_* = 0. \quad (10)$$

Due to the condition  $\sum_{i=1}^n f_i = 1$ , it holds that  $\sum_{i=1}^n \mathbf{C}_i = \mathbf{B}$  implying

$$\sum_{i=1}^n \mathbf{B}^{-1} \mathbf{C}_i = \sum_{i=1}^n \mathbf{F}_i = \mathbf{I}. \quad (11)$$

Thus, Equation (10) is satisfied, if

$$\mathbf{f}_i^T \mathbf{x}_* = y_i, \quad \text{for } i = 1, 2, \dots, n, \quad (12)$$

that is, if  $\mathbf{A}\mathbf{x}_* = \mathbf{y}$ . Consequently, an estimate of this fixed-point can be used as the reconstruction of the particle concentration distribution  $g(s)$ . The convergence of the iteration (8) can be guaranteed, if the initial guess  $\mathbf{x}_0$  is chosen appropriately which is shown in Appendix A. As the initial guess we use  $\mathbf{x}_0 = \sum_{i=1}^n y_i \mathbf{f}_i$  which is based on the assumption that the kernel functions are close-to-orthogonal, i.e.,  $\int_{s_1}^{s_2} f_\ell(s) f_j(s) ds \approx \delta_{\ell,j}$  with  $\delta_{\ell,j} = 1$  for  $\ell = j$  and  $\delta_{\ell,j} = 0$ , otherwise; with perfectly orthogonal kernels the initial guess coincides with the fixed-point. Further, when the basis functions are orthogonal (e.g., point-wise) or close-to-orthogonal (e.g., kernels),  $\mathbf{G}_k$  will be diagonal or close-to-diagonal, and  $\mathbf{x}_{k+1}$  will be non-negative provided that  $\mathbf{x}_k$  is.

### 2.3. Iterative L1 norm regularization

As a reference approach, we use an iterative L1-regularization technique, which estimates the minimizer of the objective function in the following manner:

$$\mathbf{x}^\dagger = \arg \min_{\mathbf{x}} \Psi(\mathbf{x}) \quad \text{with} \quad \Psi(\mathbf{x}) = \|\mathbf{A}\mathbf{x} - \mathbf{y}\|_2^2 + \alpha \|\mathbf{x}\|_1. \quad (13)$$

The L1 norm  $\|\mathbf{x}\|_1$  regularization function has been chosen as it tends to produce well-focused distributions and as the shape of the distribution  $g(s)$  is likely to be peaked. The estimate of  $\mathbf{x}^\dagger$  is produced via the following gradient-based iterative regularization procedure [10, 20, 21]:

$$\mathbf{x}_{\ell+1} = (\mathbf{A}^T \mathbf{A} + \frac{1}{4} \alpha^2 \mathbf{\Gamma}_\ell)^{-1} \mathbf{A}^T \mathbf{y}, \quad \mathbf{\Gamma}_\ell = \text{diag}(|\mathbf{x}_\ell| + \varepsilon)^{-1}, \quad \mathbf{\Gamma}_0 = \mathbf{I}, \quad (14)$$

where  $\alpha$  is the main regularization parameter and the role of the secondary parameter is to prevent division of one by a tiny number, i.e., that  $\mathbf{\Gamma}_\ell$  does not become ill-conditioned, if the entries of  $\mathbf{x}_\ell$  tend to zero. This iteration can be interpreted as a gradient-based optimization method which alternates between two conditional optimization steps when seeking the minimum as shown in Appendix B. In inverse problems research this iteration is known as the *iterative alternating sequential* (IAS) optimization method and it is known to usually converge within a comparably low number of iteration steps, e.g., five [22–25]. Furthermore, the reconstruction obtained can be also associated with a *maximum a posteriori* estimate for a conditionally Gaussian hierarchical Bayesian model [26]. The theory of Bayesian analysis applied to aerosol measurements can be found, e.g., in [27, 28] and its application for ELPI has been presented in [17]. The suitability of L1-regularized estimates for finding a sparse reconstruction, e.g., a concentration distribution corresponding to only a few kernels, has been presented, e.g., in [29].

### 2.4. Function bases for hardware-level implementation

We investigate the effect of two different function bases in approaching the inverse problem. The first one is formed by the smooth kernel functions, i.e.,  $f_j = \chi_j$ ,

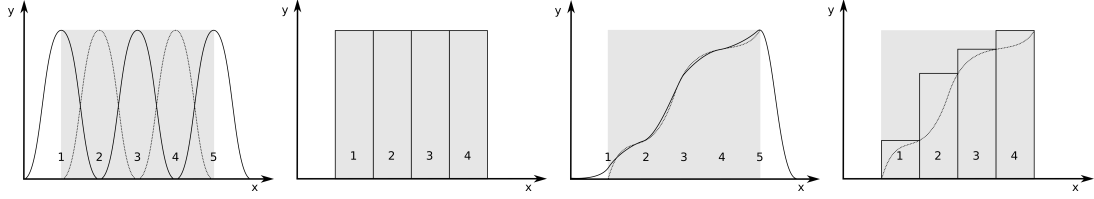


**Figure 1. 1st and 2nd from left:** The difference between the kernel and characteristic basis in representing a function defined on a one-dimensional sub-interval of the real line  $\mathbb{R}$  (gray). The smooth kernel functions (left) overlap and sum to one at each point of definition. The characteristic functions (right), in contrast, do not overlap. **3rd and 4th from left:** When approximating a given (dashed) function, a superposition of the kernel functions (left) leads to a smooth (solid) curve and the characteristic functions (right) to a staircase-like (solid) contour. As we use a finer sub-division, i.e., shorter sub-intervals, a continuous curve can be approximated also in the latter case.

$j = 1, 2, \dots, n$ , and the second one by the characteristic set-indicator basis functions (indicator functions) of the interval  $[s_1, s_2]$ , that is,  $\varphi_j = \chi_j$ ,  $i = 1, 2, \dots, m$ . The main difference between these two bases is that in the first one the basis functions overlap and the number of degrees of freedom is the same in both the measurement and reconstruction process ( $m = n$ ), whereas in the second one there is no overlap and the reconstruction process involves more degrees of freedom ( $m \gg n$ ). Namely, as depicted in Figure 1, approximating a continuous function with a piece-wise constant set of functions requires, generally, a denser set of sub-intervals compared to a smooth approximation which is obtained with the kernel functions. Figure 1 also visualizes the difference between the kernel and characteristic basis in representing a function defined on a one-dimensional sub-interval of the real line  $\mathbb{R}$ .

For the second basis, the matrix  $\mathbf{F}_i$  is diagonal, meaning that it allows for a matrix free implementation of the fixed-point iteration (8). This is an important point regarding inversion of the data using the measurement equipment, that is, a field programmable gate array (FPGA) in which evaluating a matrix-vector product requires a case-specific design [11–13].

## 2.5. Numerical experiments

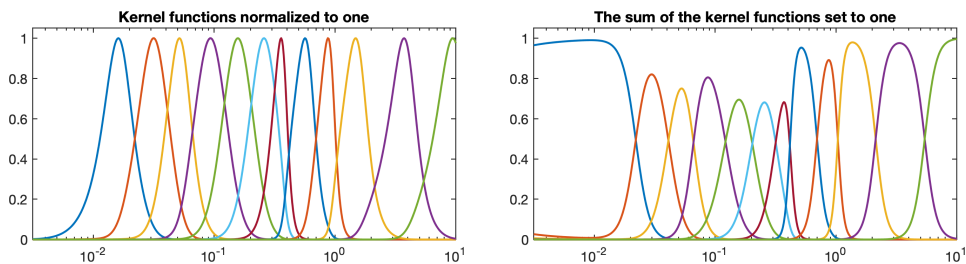


**Figure 2.** The sensitivity kernels used in the numerical experiments correspond to an actual set measured for an ELPI instrument matching with those of [16]. On the left, the sensitivity profiles of the  $\tilde{f}_1, \tilde{f}_2, \dots, \tilde{f}_n$  have been normalized to one. The kernels on the right are obtained as  $f = \tilde{f}_i(s) / \sum_{i=1}^n \tilde{f}_i(s)$ . That is, they satisfy the condition  $\sum_{i=1}^n \tilde{f}_i = 1$  for all  $s \in [s_1, s_2]$  which follows from that the total particle mass is captured by the cascade impactor due to a serial coupling of its stages and which is essential for the convergence of the proposed fixed-point iteration. **Near the end points of the investigated interval the overlap between the kernels is weak or absent. This affects the shape of the extreme kernels, when their sum is set to one (right).**

To investigate the performance of the proposed fixed-point iteration and to compare it to the outcome of the IAS algorithm, we use seven different simulated gravimetric

impactor measurements of particle mass concentration distributions, i.e., the detected mass (micrograms) per volume (cubic centimeter), as a function of the particle size (micrometer). Of these, distributions 1st – 6th are unimodal and 7th multimodal. The investigated size range varies from  $s_1 = 0.003$  to  $s_2 = 10$  micrometers. This interval was covered with twelve sensitivity kernel functions, which correspond to the kernels of *Dekati Classic ELPI* and coincide with those used in [16]. As shown in Figure 2, the kernels for the inverse computation were obtained from the separate normalized sensitivity profiles  $\tilde{f}_1, \tilde{f}_2, \dots, \tilde{f}_n$  of the cascade impactor’s stages as given by

$$f_i(s) = \frac{f_i(s)}{\sum_{i=1}^n f_i(s)}, \quad \text{for } i = 1, 2, \dots, n, \quad (15)$$

following from the assumption that the total detected mass is captured by the serially coupled impactor in which the particles not captured by the  $i$ -th stage are passed to the  $(i + 1)$ -th one.

The particle size distributions are log-normal. It is assumed that the density of matter is constant and that the particles are spherical, meaning that the eventual mass concentration follows from the particle mass density  $\rho$  multiplied by the volume of a sphere  $V = \pi s^3/6$  with the diameter  $s$ , that is,

$$g(t) = \frac{4s^3\rho}{3\sigma\sqrt{2\pi}} \exp\left(-\frac{1}{2}\left(\frac{\ln(s) - \ln(s_0)}{\sigma}\right)^2\right). \quad (16)$$

Here  $\sigma = 1.23$  defines the width of the distribution,  $s_0$  the aerosol particle mean diameter which is given the values 0.008, 0.02, 0.1, 0.8, 3, and 9 corresponding to the 1th to 6th unimodal distribution, respectively, and  $\rho = 5.11E04 \mu\text{g}/\text{m}^3$ . The 7th distribution was obtained as a superpositon of 1th to 6th with the relative weights 0, 1, 0.003, 0.001, 0.0001, and, 0, respectively. The spherical approximation for the particle shape is adopted here for its simplicity, while in reality the shape is not necessarily such. The mass distribution of particles with different but uniform shape, e.g., if they are cylindrical, can be obtained by multiplying the current one by constant.

The numerical inversion computations were performed by dividing the interval  $[s_1, s_2]$  into 500 point-wise basis functions (set-indicators of equi-length sub-intervals) which were used in evaluating all the integrals as described in Section 2.4. The data were simulated in a lattice with three times this size in order to avoid *inverse crime*, i.e., an overly good fit between the reconstruction and actual distribution [30]. The number of iteration steps was set to be 10 for both the fixed-point and IAS method.

**Table 1.** The relative level of zero-mean Gaussian white noise in the numerical experiments measured via standard deviation (STD) vs. noiseless data amplitude and expected noise vs. noiseless data L2 norm.

Distribution	Type	Relative to	Noise level (%)				
1–7	all	amplitude	1.0	1.5	2.0	2.5	3.0
1	unimodal	L2 norm	3.5	5.2	6.9	8.7	10.4
2	unimodal	L2 norm	2.6	3.9	5.2	6.5	7.7
3	unimodal	L2 norm	2.8	4.2	5.6	7.0	8.4
4	unimodal	L2 norm	2.5	3.8	5.0	6.7	7.5
5	unimodal	L2 norm	3.0	4.5	6.0	7.6	9.1
6	unimodal	L2 norm	3.5	5.2	6.9	8.7	10.4
7	multimodal	L2 norm	2.1	3.1	4.2	5.2	6.2

The performance of the fixed-point and IAS iteration were evaluated in three different inversion tests. In the first one (**I**), in order to evaluate the overall accuracy of



the inverse approaches, a constant noise standard deviation (STD), 1.5 % of the maximum entry in the noiseless simulated data vector, was used and the reconstructions obtained were analyzed visually as distributions. In the second one (**II**), to find the robustness of the inversion, a sample of reconstructions was generated for 100 different noise realizations and the noise STDs of 1.0, 1.5, 2.0, 2.5, and 3.0 % with respect to the noiseless data amplitude. The corresponding relative noise levels with respect to the L2 norm of the noiseless data are included in Table 1.

Based on these noise levels, the L1-regularization parameter of the IAS method was chosen to be  $\alpha = 2.0\text{E-}04$ . With this choice, the value of the penalty function  $\alpha\|\mathbf{x}\|_1$  in (13) for a normalized distribution  $\|\mathbf{x}\|_1 = 1$  will be approximately the expected noise fluctuation of  $\|\mathbf{Ax} - \mathbf{y}\|_2^2$ , when the standard deviation of the noise in relation to its L2 norm is 1.4 %. Consequently, the discrepancy of the regularization will be close to that of the noise without exceeding it, the relative difference to the lowest noise level 2.1 % in L2 norm (Table 1) being approximately 50 %.

We analyze the results via box-plots showing the following relative L1 norm  $\|\cdot\|_1$  and, as a complementary measure, the infinity norm  $\|\cdot\|_{\text{inf}}$  difference between the original distribution  $g$  and its reconstruction  $g_*$ :

$$\frac{\|g - g_*\|_1}{\|g\|_1} = \frac{\int |g(s) - g_*(s)| ds}{\int |g(s)| ds} \quad (17)$$

$$\frac{\|g - g_*\|_{\text{inf}}}{\|g\|_{\text{inf}}} = \frac{\max_{s \in [s_1, s_2]} |g(s) - g_*(s)|}{\max_{s \in [s_1, s_2]} |g(s)|}. \quad (18)$$

L1 and infinity norm can be interpreted as the two extreme cases of Lp norm, as  $\|\cdot\|_p \leq \|\cdot\|_q$ , if  $1 \leq q \leq p \leq \infty$ . The L1 norm represents the sum of the absolute differences over all entries in the reconstructed distribution, while the infinity norm corresponds to the point-wise maximum absolute error. As a complementary test, a synthetic multimodal distribution was reconstructed and analyzed via the approach of (**I**) and (**II**) to validate the results obtained with the unimodal distributions.

### 3. Results

The principal results of the numerical experiments (**I**) and (**II**) can be found included in Figures 3, 4, respectively. Table 2 shows the total floating point operations (FLOP) and peak memory consumption corresponding to each inversion method. The complementary results have been included in Figures C1 and C2 in Appendix C. The Matlab (The Mathworks Inc.) code applied to obtain the results is openly available<sup>1</sup>.

**Table 2.** The total floating point operations (FLOP) and peak memory consumption corresponding to each inversion method, when the number of points in the final one-dimensional point lattice of the reconstruction is 25, 50, 100, and 500.

points	Pointwise				Kernel			
	Fixed-point		L1-regularized		Fixed-point		L1-regularized	
	kFLOP	Mem. (kB)	kFLOP	Mem. (kB)	kFLOP	Mem. (kB)	kFLOP	Mem. (kB)
25	4.19	3.95	15.3	9.36	2.80	3.95	4.68	5.10
50	7.79	7.75	52.8	28.6	3.40	7.75	5.28	8.90
100	15.0	15.4	195	97.0	3.23	15.4	6.48	16.5
500	72.6	76.2	4580	2080	16.1	76.2	14.1	77.3

<sup>1</sup>[https://github.com/sampsapursiainen/cascade\\_impactor\\_inversion](https://github.com/sampsapursiainen/cascade_impactor_inversion)

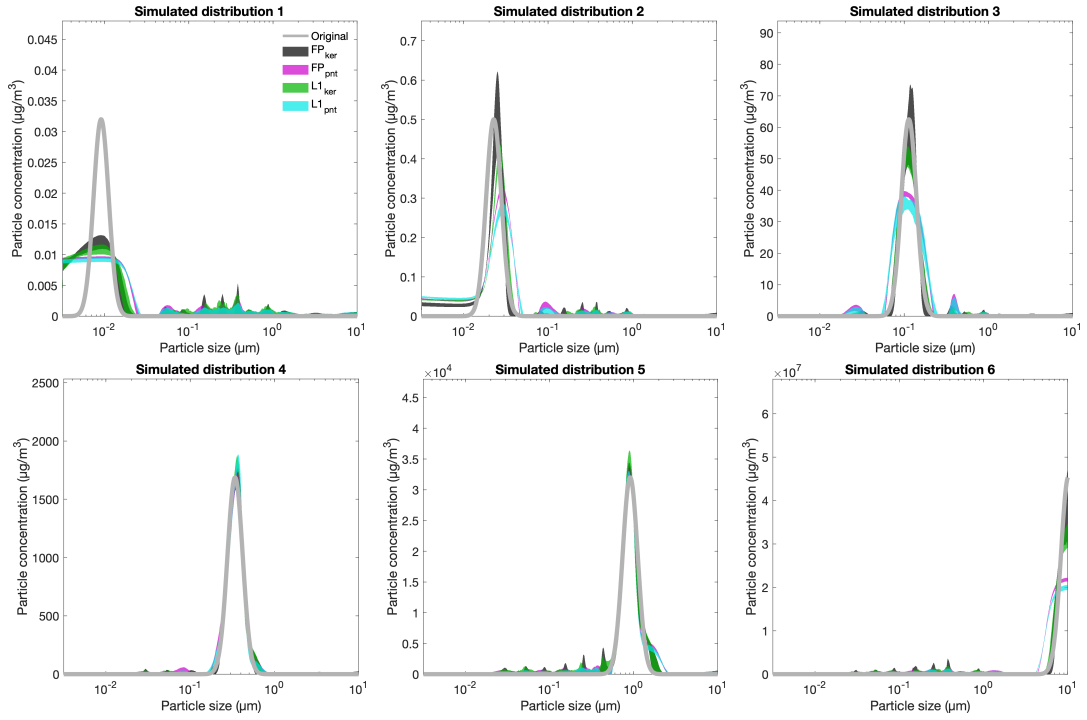


**Figure 3.** The results of the numerical experiment (I) obtained with a constant 1.5 % noise level w.r.t. the data amplitude for a sample 100 of reconstructions corresponding to different noise vector realizations. The solid gray line depicts the original aerosol distribution which is approximated by the sub-interval- and kernel-based (pnt and ker) reconstructions obtained with the fixed-point (F-P) iteration and IAS L1-regularization (L1) method. The effect of noise is clearly visible as secondary peaks next to the primary peak. For each reconstruction type, the area visualized shows the interdecile range, i.e., the interval between 10 and 90 % quantile.

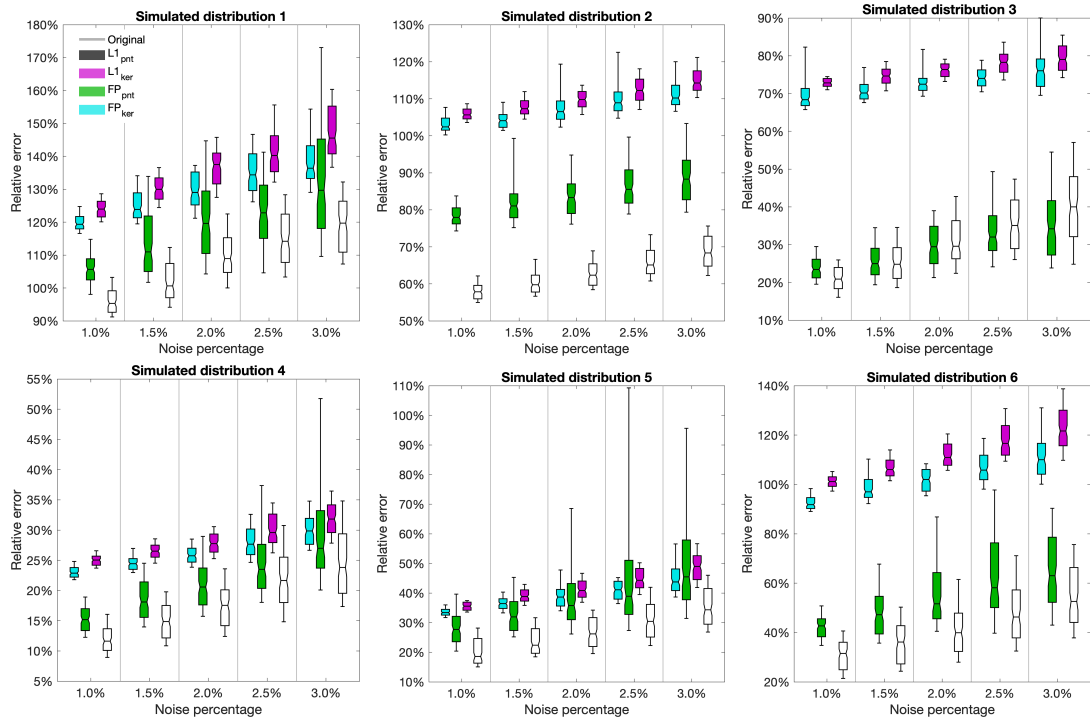


**Figure 4.** The relative L1 norm difference (17) between the original distribution and its reconstruction obtained in the numerical experiment (II) obtained with the variable 1.0 – 3.0 % noise level w.r.t. the data amplitude. At each level, a sample of 100 reconstructions corresponding to different noise vector realizations was generated for altogether four cases using the fixed-point (FP) iteration and IAS L1-regularization (L1) method and the sub-interval- and kernel-based (pnt and ker) approaches. In each box-plot, the thicker part of the box-plot shows the interquartile range (25 to 75 % quantile) and the upper and lower whisker show the interdecile range (10 to 90 % quantile), respectively, containing the outliers of the sample obtained.

In **(I)**, we analyzed the interdecile range, i.e., the interval between 10 and 90 % quantile, of the reconstructed distributions for each simulated aerosol particle concentration distribution (Figure 3). The point-wise basis functions provided more consistent reconstruction quality compared to the kernel basis. The point-wise reconstructions found a more refined peak for the distributions 1, 2, 3, and 6 in which the maximum is located near or at an end point of the interval, whereas the kernel-based estimates seem more regular and less peaked. This can be interpreted to follow from the span of the kernel basis, which towards the end points becomes limited due to a decreasing number of overlapping kernels. For distribution 1, the overlap is absent at the peak (Figure 2) and, consequently, none of the distributions decay to zero. In addition there are artifacts or side peaks which occur at the locations, where one or more of the kernels vanish. These are somewhat pronounced in the point-wise case as compared to the kernel based reconstructions. For the distributions 4 and 5, the point and kernel basis resulted in a similar performance.

The results of **(II)** presented in Figure 4 suggest that with a noise level below 3.0 % w.r.t. the maximum amplitude of the signal, the relative errors obtained with the point-wise basis were generally smaller than what was obtained with the kernel basis. The point-wise basis, however, also corresponds to a larger error spread, i.e., the interquartile range (25 to 75 % quantile), which also grows faster along with the noise level. Furthermore, the fixed-point and IAS method perform differently with respect to increasing noise with the latter one of these being more robust; the outliers in the relative error for the fixed-point iteration grow notably in the case of the point-wise basis as the noise increases. The point-wise IAS L1-regularization provided overall the smallest error level in the numerical experiments.

The complementary results (Figure C1) obtained for the infinity norm show the maximum point-wise difference between the actual and reconstructed distribution which was observed to include enhanced outliers compared to the case of the L1 norm. The complementary test with the multimodal distribution (Figure C2) led to a somewhat improved accuracy and suppressed outliers as compared to the unimodal case, suggesting that the unimodal results represent the overall performance of the present methods appropriately.

#### 4. Discussion

This study focused on inverting cascade impactor measurements [1]. We introduced and analyzed a fixed-point iteration for inverting simulated cascade impactor measurement data for seven different aerosol size distributions using a set of sensitivity kernel functions corresponding to an ELPI instrument. It was shown that with an appropriate initial guess and regular enough sensitivity kernel functions, the iteration converges towards the original distribution. Furthermore, the algorithm can be formulated in a matrix-free form via a point-wise approach, in which the sub-intervals of the investigated particle size-range provide the function basis for solving the inverse problem. The results were compared to the performance of the IAS iteration technique [22–25] which – as an L1-regularized approach – is advantageous for reconstructing sparse distributions [29]. These inversion approaches were compared by using the sensitivity kernels as the inverse function basis. The robustness of the fixed-point and IAS techniques were analyzed using different noise levels.

Our central finding is that when the relative errors in the measurements are below 3 % of the maximal data entry for the most loaded stages, the fixed-point approach

has a superior accuracy. For a gravimetric measurement such an uncertainty level has been achieved, e.g., in with a 300  $\mu\text{g}$  loading and 10  $\mu\text{g}$  resolution [31] which can generally vary between 0.01 and 10  $\mu\text{g}$  in different measurement equipment [2]. In the case of a electrometric measurement, the error refers to the current measured by the cascade impactor, which in the recent study [4] has been estimated to be of the order 1 % for the ELPI+ instrument<sup>2</sup> (Dekati Ltd.). The electric currents measured by the electrometers depend on uncertainties in the particle concentration and flow which, in [4], are estimated to be 3 % and 1 %, respectively following from the performance of the particle charger. Assuming that each of these uncertainties are Gaussian, i.e., by considering the root of the sum of the squares as the total measure, the eventual measurement uncertainty will be about 3.3 %.

In this study, the IAS algorithm was found to be more robust with respect to the noise than the fixed-point iteration. Hence, IAS might be a preferable for applications, where the noise significantly exceeds the 3.0 % error level w.r.t. the data amplitude. Our finding is in agreement with the recent study [15], which utilizes an inversion principle similar to the present fixed-point approach without an accurate mathematical formulation or proof of its convergence, and suggests that the noise effects will become visible with measurement errors around 5 % or above. In [15], the inversion errors were also observed to grow towards the end point of the investigated particle size range. Based on the present formulation and results, this latter finding is an obvious consequence of the vanishing kernel function overlap in the vicinity of the end points, meaning that the partition of unity condition (Section 2.1) is not satisfied; when the kernel functions do not form a partition of unity, the inversion method does not converge, and the errors obtained are likely to be large and highly case-specific, i.e., difficult to be predicted.

The point-wise reconstruction approach was found to be advantageous with respect to maintaining the inversion quality in the vicinity of the end points. Consequently, the point-wise approach can be seen as superior to using the kernel functions as the function basis for the inverse problem. The errors of the point-wise reconstructions were observed to occur particularly at the points, where one or more kernel functions vanish, while the kernel-based reconstructions were observed to be biased by kernel shape. Generally, the total error of the cascade impactor measurement depends on both measurement noise and modelling errors of which the latter are affected by factors such as the variance in particle density and morphology, dirtiness of the impactor, and humidity, and are reflected in the accuracy of the kernel functions. A total relative error of 20 % has been estimated for sub-micrometer particulates.

The present zero-mean Gaussian white noise model is well-justified in the current context of numerical analysis, as it can be interpreted as an approximation of a zero-mean random error with a given second moment, without specifying whether the error is due to measurements or modelling, and as uncorrelated errors can be related to both the amplitude and L2 norm of the noiseless data in a straightforward manner. Gaussian noise has previously been utilized in the mathematical inversion of aerosol distributions, e.g., in [19]. However, the Poisson-Gaussian model which is more accurate with respect to the detected particle counts can be considered more advantageous for a real application [32, 33].

When implemented using the point-wise basis, the proposed fixed-point technique is significantly simpler than the IAS iteration, which is obvious by comparing the total FLOPs and memory consumption of these two methods. We deem that the most

---

<sup>2</sup><https://www.dekati.com/products/elpi/>

significant advantage of the fixed-point method is its matrix-free formulation. The ability to perform matrix-free computations is essential with respect to instrument-based inversion of the measurements due to the limited computing capability of the instrument's own hardware, e.g., an field programmable gate array (FPGA) board. FPGAs are based on a block architecture, where larger operations are subdivided in smaller entities performed by digital signal processor (DSP) blocks [34] utilizing block random access memory BRAM ranging from 8Kb to 256Kb per block [35], thus limiting the performance of the linear algebraic operations involving large matrices. In [36], FPGA-based matrix-vector multiplications with computational have been suggested to have the peak clock speed of about 24,000 kHz and 680 kHz per DSP block (DSP48E 23x28 multiplier) for matrix dimensions 500-by-500 and 10-by-10, when parallelized using 500 and 10 blocks, respectively, together with one BRAM block per DSP. As each simulated DSP block performs 2 FLOP per cycle, the resulting total simulated performance is about 480 MFLOP/s and 680 MFLOP/s, respectively.

These two cases can be considered as a reference for the point-wise fixed-point and IAS iteration, respectively. Since the former case is matrix-free, the number of parallel processes would be determined by the number of kernel functions (here 12), while the latter case necessitates matrix-vector multiplications for a matrix dimension following from the number of points in the one-dimensional lattice (here 500). Moreover, as the matrix-free method can be implemented effectively with only a few blocks, it can be considered preferable in low-cost and low-power hardware implementation. For example, Intel Cyclone 10 LP 10CL025, which can be operated with 1.0 and 1.2 V core voltage, would provide a provide a potential platform for such an implementation with its 66 DSP blocks and 594 kb (66x9 kB) of BRAM.

The future work might involve investigating efficient hardware-level FPGA implementations of the present fixed-point approach. A deeper investigation on the effect of the kernel regularity on the inversion quality might be conducted, as the shape of the kernels was here reflected in the reconstructions, especially, at the lower end of the particle size range. Finally, the robustness of the inversion might be improved via statistical reconstruction approaches, e.g., Markov chain Monte Carlo methodology [37], interpreting that the IAS technique follows from the hierarchical Bayesian model which can be approached via sampling.

## 5. Conclusion

This study introduced and evaluated mathematically a fixed-point iteration for inverting cascade impactor measurements. The inversion outcome provided by this iteration was found to be robust with for a noise level below 3.0 % w.r.t. the maximum amplitude which can be achieved in practical applications including both gravimetric and electrometric measurements. Using a point-wise function basis, the proposed technique allows a matrix-free implementation which is advantageous with respect to hardware-level computations performed in an FPGA board. Furthermore, the point-wise basis was observed to be preferable with respect to maintaining the inversion accuracy in near the boundary points of the investigated particle size range.

## Acknowledgements

This work was supported by the AoF Centre of Excellence in Inverse Modelling and Imaging 2018-2025.

## References

- [1] Kulkarni, Pramod, Baron PA, et al. Aerosol measurement. Wiley; 2011.
- [2] Hinds W. Aerosol technology: Properties, behavior, and measurement of airborne particles. Wiley; 2012.
- [3] Keskinen J, Pietarinen K, Lehtimäki M. Electrical low pressure impactor. *Journal of Aerosol Science*. 1992;23(4):353–360.
- [4] Järvinen A, Aitomaa M, Rostedt A, et al. Calibration of the new electrical low pressure impactor (elpi+). *Journal of aerosol science*. 2014;69:150–159.
- [5] Arffman A, Yli-Ojanperä J, Kalliokoski J, et al. High-resolution low-pressure cascade impactor. *Journal of Aerosol Science*. 2014;78:97–109.
- [6] Yli-Ojanperä J, Kannosto J, Marjamäki M, et al. Improving the nanoparticle resolution of the elpi. *Aerosol and Air Quality Research*. 2010;10(4):360–366.
- [7] Amaral S, de Carvalho J, Costa M, et al. An overview of particulate matter measurement instruments. *Atmosphere*. 2015;6(9):1327–1345.
- [8] Virtanen AK, Ristimäki JM, Vaaraslahti KM, et al. Effect of engine load on diesel soot particles. *Environmental science & technology*. 2004;38(9):2551–2556.
- [9] Maricq MM, Xu N, Chase RE. Measuring particulate mass emissions with the electrical low pressure impactor. *Aerosol Science and Technology*. 2006;40(1):68–79.
- [10] Kaipio JP, Somersalo E. Statistical and computational methods for inverse problems. Berlin: Springer; 2004.
- [11] Lee TC, White M, Gubody M. Matrix multiplication on fpga-based platform. In: *Proceedings of the World Congress on Engineering and Computer Science*; Vol. 1; 2013.
- [12] Kestur S, Davis JD, Chung ES. Towards a universal FPGA matrix-vector multiplication architecture. In: *2012 IEEE 20th International Symposium on Field-Programmable Custom Computing Machines*; IEEE; 2012. p. 9–16.
- [13] Jang JW, Choi SB, Prasanna VK. Energy-and time-efficient matrix multiplication on FPGAs. *IEEE Transactions on Very Large Scale Integration (VLSI) Systems*. 2005;13(11):1305–1319.
- [14] Hoffman JD, Frankel S. *Numerical methods for engineers and scientists*. CRC press; 2001.
- [15] Saari S, Arffman A, Harra J, et al. Performance evaluation of the hr-elpi+ inversion. *Aerosol Science and Technology*. 2018;52(9):1037–1047.
- [16] Marjamäki M, Lemmetty M, Keskinen J. ELPI response and data reduction i: Response functions. *Aerosol Science and Technology*. 2005;39(7):575–582.
- [17] Lemmetty M, Keskinen J, Marjamäki M. The ELPI response and data reduction ii: Properties of kernels and data inversion. *Aerosol science and technology*. 2005;39(7):583–595.
- [18] Winklmayr W, Wang HC, John W. Adaptation of the twomey algorithm to the inversion of cascade impactor data. *Aerosol Science and Technology*. 1990;13(3):322–331.
- [19] Gulak Y, Jayjock E, Muzzio F, et al. Inversion of andersen cascade impactor

- data using the maximum entropy method. *Aerosol Science and Technology*. 2010; 44(1):29–37.
- [20] Pursiainen S, Kaasalainen M. Detection of anomalies in radio tomography of asteroids: Source count and forward errors. *Planetary and Space Science*. 2014; 99(0):36 – 47.
- [21] Pursiainen S, Kaasalainen M. Sparse source travel-time tomography of a laboratory target: accuracy and robustness of anomaly detection ; 2014.
- [22] Calvetti D, Somersalo E. Introduction to Bayesian scientific computing – Ten lectures on subjective computing. New York: Springer Verlag; 2007.
- [23] Calvetti D, Hakula H, Pursiainen S, et al. Conditionally gaussian hypermodels for cerebral source localization. *SIAM J Imaging Sci*. 2009;2(3):879–909.
- [24] Pursiainen S, Kaasalainen M. Iterative alternating sequential (IAS) method for radio tomography of asteroids in 3D. *Planetary and Space Science*. 2013;78.
- [25] Calvetti D, Somersalo E, Strang A. Hierarchical bayesian models and sparsity: 2-magic. *Inverse Problems*. 2019;35(3):035003.
- [26] O’Hagan A, Forster F. Kendall’s advanced theory of statistics, volume 2b: Bayesian inference. London: Arnold; 2004.
- [27] Ramachandran G, Kandlikar M. Bayesian analysis for inversion of aerosol size distribution data. *Journal of aerosol science*. 1996;27(7):1099–1112.
- [28] Voutilainen A, Kolehmainen V, Kaipio J. Statistical inversion of aerosol size measurement data. *Inverse Problems in Engineering*. 2001;9(1):67–94.
- [29] Donoho DL. For most large underdetermined systems of equations, the minimal  $\ell_1$ -norm near-solution approximates the sparsest near-solution. *Communications on Pure and Applied Mathematics: A Journal Issued by the Courant Institute of Mathematical Sciences*. 2006;59(7):907–934.
- [30] Colton D, Kress R. Inverse acoustic and electromagnetic scattering theory. Springer; 1998. Applied Mathematical Sciences.
- [31] Pagels J, Gudmundsson A, Gustavsson E, et al. Evaluation of aerodynamic particle sizer and electrical low-pressure impactor for unimodal and bimodal mass-weighted size distributions. *Aerosol Science and Technology*. 2005;39(9):871–887.
- [32] Foi A, Trimeche M, Katkovnik V, et al. Practical poissonian-gaussian noise modeling and fitting for single-image raw-data. *IEEE Transactions on Image Processing*. 2008;17(10):1737–1754.
- [33] Sipkens TA, Hadwin PJ, Grauer SJ, et al. General error model for analysis of laser-induced incandescence signals. *Applied optics*. 2017;56(30):8436–8445.
- [34] Ronak B, Fahmy SA. Mapping for maximum performance on fpga dsp blocks. *IEEE Transactions on Computer-Aided Design of Integrated Circuits and Systems*. 2015;35(4):573–585.
- [35] Yazdanshenas S, Tatsumura K, Betz V. Don’t forget the memory: Automatic block ram modelling, optimization, and architecture exploration. In: *Proceedings of the 2017 ACM/SIGDA International Symposium on Field-Programmable Gate Arrays*; 2017. p. 115–124.
- [36] Abbaszadeh A, Iakymchuk T, Bataller-Mompeán M, et al. An scalable matrix computing unit architecture for fpga, and scumo user design interface. *Electronics*. 2019;8(1):94.
- [37] Liu J. Monte carlo strategies in scientific computing. Springer Verlag GmbH; 2001. Springer Series in Statistics.
- [38] O’Searcoid M. Metric spaces. Springer Science & Business Media; 2006.
- [39] Rudin W. Real and complex analysis. Tata McGraw-hill education; 2006.



## 6. Appendices

### Appendix A. Convergence of the fixed-point iteration

This section shows that if the initial guess for (8) is accurate enough, the iteration will converge to the fixed-point  $\mathbf{x}_*$ . To prove the convergence, it is sufficient to show that the Lipschitz condition of order one is satisfied for  $G$ , i.e., that  $G$  is Lipschitz continuous [38, 39],

$$\|\mathbf{x}_{k+1} - \mathbf{x}_k\| = \|G(\mathbf{x}_k) - G(\mathbf{x}_{k-1})\| \leq q\|\mathbf{x}_k - \mathbf{x}_{k-1}\| \quad (\text{A1})$$

with the Lipschitz constant  $q < 1$  for  $k \geq K \geq 1$ . Namely, then  $\|\mathbf{x}_{k+\ell+1} - \mathbf{x}_{k+\ell}\| \leq q^{\ell+1}\|\mathbf{x}_k - \mathbf{x}_{k-1}\| \rightarrow 0$ , if  $\ell \rightarrow T$ . This condition can hold only if the number of the kernel functions is equal to or larger than that of the basis functions, i.e., if  $n \geq m$ . Otherwise, there exist a nonzero  $\mathbf{x}$  such that  $\mathbf{f}_i^T \mathbf{x} = 0$  for some  $i = 1, 2, \dots, n$  meaning that the function  $G(\mathbf{x})$  will be singular. When  $n \geq m$ ,  $G(\mathbf{x})$  is smooth and the center value theorem implies that the following equation is satisfied for some  $\mathbf{z} = \mathbf{x}_k + \xi_0(\mathbf{x}_{k+1} - \mathbf{x}_k)$  with  $0 \leq \xi_0 \leq 1$ :

$$G(\mathbf{x}_{k+1}) - G(\mathbf{x}_k) = \tilde{G}'(\xi_0), \quad (\text{A2})$$

where  $\tilde{G}(\xi) = G(\mathbf{x}_k + \xi(\mathbf{x}_{k+1} - \mathbf{x}_k))$ , that is,

$$\tilde{G}(\xi) = \sum_{i=1}^n \frac{y_i (\mathbf{F}_i \mathbf{x}_k + \xi \mathbf{F}_i (\mathbf{x}_{k+1} - \mathbf{x}_k))}{\mathbf{f}_i^T \mathbf{x}_k + \xi \mathbf{f}_i^T (\mathbf{x}_{k+1} - \mathbf{x}_k)} \quad (\text{A3})$$

and

$$\begin{aligned} \tilde{G}'(\xi_0) &= \sum_{i=1}^n \left( -\frac{\mathbf{f}_i^T (\mathbf{x}_{k+1} - \mathbf{x}_k) y_i (\mathbf{F}_i \mathbf{x}_k + \xi \mathbf{F}_i (\mathbf{x}_{k+1} - \mathbf{x}_k))}{(\mathbf{f}_i^T \mathbf{x}_k + \xi \mathbf{f}_i^T (\mathbf{x}_{k+1} - \mathbf{x}_k))^2} \right. \\ &\quad \left. + \frac{y_i \mathbf{F}_i (\mathbf{x}_{k+1} - \mathbf{x}_k)}{\mathbf{f}_i^T \mathbf{x}_k + \xi \mathbf{f}_i^T (\mathbf{x}_{k+1} - \mathbf{x}_k)} \right) \end{aligned} \quad (\text{A4})$$

$$= \sum_{i=1}^n \frac{y_i}{(\mathbf{f}_i^T \mathbf{z})^2} ((\mathbf{f}_i^T \mathbf{z}) \mathbf{F}_i - \mathbf{F}_i \mathbf{z} \mathbf{f}_i^T) (\mathbf{x}_{k+1} - \mathbf{x}_k) \quad (\text{A5})$$

Since  $y_i/(\mathbf{f}_i^T \mathbf{z}) \rightarrow 1$  and  $\sum_{i=1}^n \mathbf{F}_i = \mathbf{I}$ , this tends to

$$\begin{aligned} \tilde{G}'(\xi_0) &= (\mathbf{I} - \sum_{i=1}^n \frac{1}{y_i} \mathbf{F}_i \mathbf{z} \mathbf{f}_i^T + \mathbf{E})(\mathbf{x}_{k+1} - \mathbf{x}_k) \\ &= \mathbf{B}^{-1} (\mathbf{B} - \sum_{i=1}^n \frac{1}{y_i} \mathbf{C}_i \mathbf{z} \mathbf{f}_i^T + \mathbf{B}\mathbf{E})(\mathbf{x}_{k+1} - \mathbf{x}_k), \end{aligned} \quad (\text{A6})$$

where  $\mathbf{E} \rightarrow \mathbf{0}$  as  $\mathbf{x}_k \rightarrow \mathbf{x}_*$ . Assuming that the basis functions have been scaled so that  $\|\mathbf{z}\|_1 \leq \max_i(y_i) \|\mathbf{f}_i\|_1$ , it holds that

$$\|(\mathbf{B} - \sum_{i=1}^n \frac{1}{y_i} \mathbf{C}_i \mathbf{z} \mathbf{f}_i^T)(\mathbf{x}_{k+1} - \mathbf{x}_k)\|_1 \leq (1-\nu) \|\mathbf{B}(\mathbf{x}_{k+1} - \mathbf{x}_k)\|_1. \quad (\text{A7})$$

Denoting  $\mathbf{u}_k = \mathbf{B}\mathbf{x}_k$ , one can write

$$\begin{aligned} \|\mathbf{u}_{k+2} - \mathbf{u}_{k+1}\|_1 &= \|\mathbf{B}(\mathbf{x}_{k+2} - \mathbf{x}_{k+1})\|_\infty \leq (1-\nu) \|\mathbf{B}(\mathbf{x}_{k+1} - \mathbf{x}_k)\|_1 \\ &= (1-\nu) \|\mathbf{u}_{k+1} - \mathbf{u}_k\|_1, \end{aligned} \quad (\text{A8})$$

implying that the sequence  $\langle \mathbf{u}_k \rangle_{k=1}^\infty$  converges. Thus, by the invertibility of  $\mathbf{B}$  so does also  $\langle \mathbf{x}_k \rangle_{k=1}^\infty$  with  $\mathbf{x}_*$  being the limit.

## Appendix B. Convergence of the L1 norm regularized iteration

This convergence of the iteration (14) can be justified via alternating conditional minimization of the function given by

$$\begin{aligned} H(\mathbf{x}, \mathbf{z}) &= \|\mathbf{A}\mathbf{x} - \mathbf{y}\|_2^2 + \frac{1}{4}\alpha^2 \|\text{diag}(\mathbf{z})^{-1}\mathbf{x}\|_2^2 + \sum_{j=1}^M z_j \\ &= \|\mathbf{A}\mathbf{x} - \mathbf{y}\|_2^2 + \frac{1}{4}\alpha^2 \sum_{j=1}^M \frac{x_j^2}{z_j} + \frac{1}{4}\alpha^2 \sum_{j=1}^M z_j, \end{aligned} \quad (\text{B1})$$

where  $z_j > 0$ , for  $i = 1, 2, \dots, M$ . Since  $H(\mathbf{x}, \mathbf{z})$  is a quadratic function with respect to  $\mathbf{x}$ , the conditional minimizer  $\mathbf{x}^\dagger = \arg \min_{\mathbf{x}} H(\mathbf{x} | \mathbf{z})$  can be obtained through the formula

$$\mathbf{x}^\dagger = (\mathbf{A}^T \mathbf{A} + \frac{1}{4}\alpha^2 \mathbf{\Gamma}_{\mathbf{z}})^{-1} \mathbf{A}^T \mathbf{y}, \quad \mathbf{\Gamma}_{\mathbf{z}} = \text{diag}(\mathbf{z})^{-1} \quad \text{and} \quad \mathbf{\Gamma}_0 = \mathbf{I} \quad (\text{B2})$$

Furthermore, for the conditional minimizer  $\mathbf{z}^\dagger = \arg \min_{\mathbf{z}} H(\mathbf{z} | \mathbf{x})$ , the gradient of  $H(\mathbf{z} | \mathbf{x})$  is zero with respect to  $\mathbf{z}$ , that is,

$$\left. \frac{\partial H(\mathbf{x}, \mathbf{z})}{\partial z_j} \right|_{\mathbf{z}^\dagger} = -\frac{1}{4}\alpha^2 \frac{x_j^2}{(z_j^\dagger)^2} + 1 = 0, \quad \text{i.e.} \quad z_j^\dagger = |x_j| \frac{1}{2}\alpha. \quad (\text{B3})$$

It follows that the minimum can be sought via the following alternating optimization steps.

- (1) Set  $\mathbf{z}_0 = (1, 1, \dots, 1)$ ,  $\ell = 1$  and repeat the following two steps for a desired total step count.
- (2) Find  $\mathbf{x}_\ell = \arg \min_{\mathbf{x}} H(\mathbf{x}, \mathbf{z}_{\ell-1})$ .
- (3) Find  $\mathbf{z}_\ell = \arg \min_{\mathbf{z}} H(\mathbf{x}_\ell, \mathbf{z})$ .

If  $(\mathbf{x}_\ell, \mathbf{z}_\ell)$  is a global minimizer of  $H(\mathbf{x}, \mathbf{z})$ , then  $\mathbf{x}_\ell = \mathbf{x}^\dagger$ . Namely, in that case it holds that  $(z_\ell)_j = |(x_\ell)_j|$ ,  $j = 1, 2, \dots, M$ , and one can write  $\Psi(\mathbf{x}) = H(\mathbf{x}_\ell, \mathbf{z}_\ell) =$

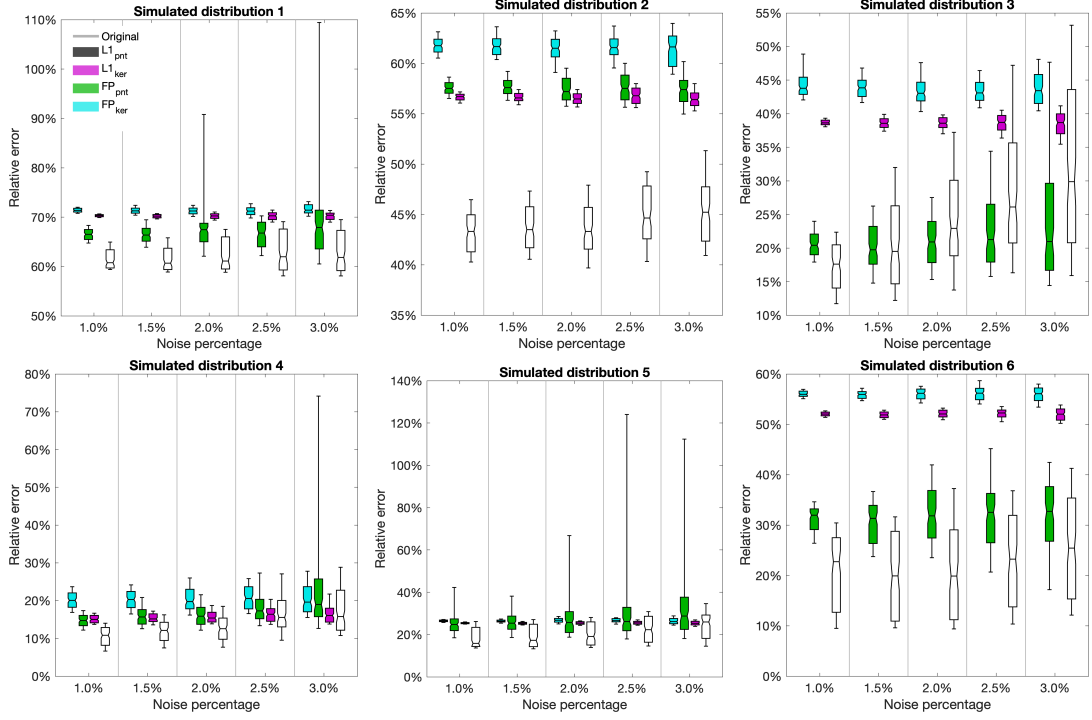


**Figure C1.** The relative infinity norm difference (18) between the original distribution and its reconstruction obtained in the numerical experiment (II) obtained with the variable 1.0 – 3.0 % noise level w.r.t. the data amplitude. At each level, a sample of 50 reconstructions to different noise vector realizations was generated for altogether four cases using the fixed-point (FP) iteration and IAS L1-regularization (L1) method and the sub-interval- and kernel-based (pnt and ker) approaches. In each box-plot, the thicker part of the box-plot shows the interquartile range (25 to 75 % quantile) and the upper and lower whisker show the interdecile range (10 to 90 % quantile), respectively, containing the outliers of the sample obtained.

$H(x_1, x_2, \dots, x_M, |x_j|, |x_j|, \dots, |x_M|)$ . Consequently, it follows that:

$$\begin{aligned}
H(\mathbf{x}_\ell, \mathbf{z}_\ell) &= \|\mathbf{Ax} - \mathbf{y}\|_2^2 + \frac{1}{4}\alpha^2 \sum_{j=1}^M \frac{x_j^2}{z_j} + \sum_{j=1}^M z_j \\
&= \|\mathbf{Ax} - \mathbf{y}\|_2^2 + \frac{1}{4}\alpha^2 \sum_{j=1}^M \frac{x_j^2}{|x_j| \frac{1}{2}\alpha} + \sum_{j=1}^M |x_j| \frac{1}{2}\alpha \\
&= \|\mathbf{Ax} - \mathbf{y}\|_2^2 + \alpha \|\mathbf{x}\|_1 = \Psi(\mathbf{x}).
\end{aligned} \tag{B4}$$

## Appendix C. Complementary results

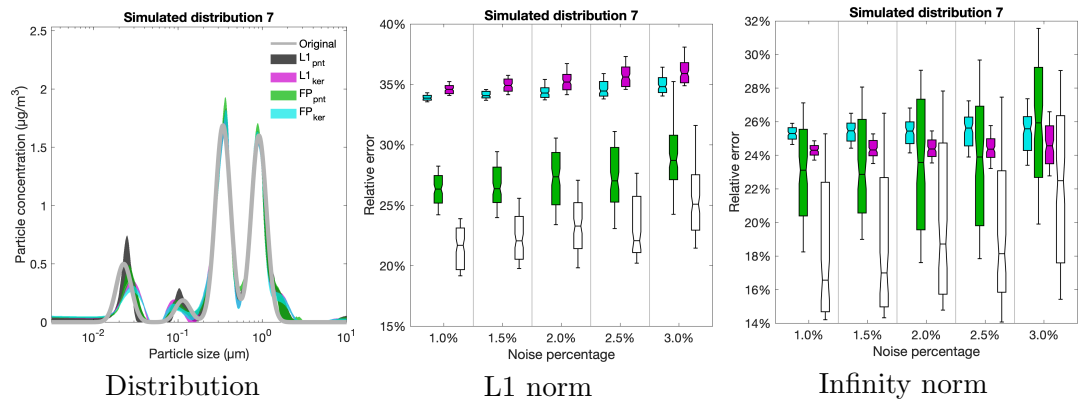


**Figure C2.** Complementary results obtained with a synthetic multimodal distribution 7. **1st from left:** The interdecile range (10 to 90 % quantile) obtained for a sample 100 of reconstructions corresponding to different noise vector realizations (1.5 % noise level w.r.t. the data amplitude). **2nd and 3rd from left:** The relative L1 and infinity norm difference (18) between the original distribution and its reconstruction obtained with the variable 1.0 – 3.0 % noise w.r.t. the data amplitude, respectively. The bar and whiskers show the interquartile and interdecile range (25 to 75 % and 10 to 90 % quantile), respectively.